Snowmelt controls on concentration-discharge relationships and the balance of oxidative and acid-base weathering fluxes in an alpine catchment, East River, Colorado

Matthew J. Winnick

Rosemary W. H. Carroll

Kenneth H. Williams

Reed M. Maxwell

Wenming Dong
Kate Maher
First published: 02 March 2017

https://doi.org/10.1002/2016WR019724

Abstract

Although important for riverine solute and nutrient fluxes, the connections between biogeochemical processes and subsurface hydrology remain poorly characterized. We investigate these couplings in the East River, CO, a high-elevation shale-dominated catchment in the Rocky Mountains, using concentration-discharge (C-Q) relationships for major cations, anions, and organic carbon. Dissolved organic carbon (DOC) displays a positive C-Q relationship with clockwise hysteresis, indicating mobilization and depletion of DOC in the upper soil horizons and emphasizing the importance of shallow flow paths during snowmelt. Cation and anion concentrations demonstrate that carbonate weathering, which dominates solute fluxes, is promoted by both sulfuric acid derived from pyrite oxidation in the shale bedrock and carbonic acid derived from subsurface respiration. Sulfuric acid weathering dominates during base flow conditions when waters infiltrate below the inferred pyrite oxidation front, whereas carbonic acid weathering plays a dominant role during snowmelt as a result of shallow flow paths. Differential C-Q relationships between solutes suggest that infiltrating waters approach calcite saturation

before reaching the pyrite oxidation front, after which sulfuric acid reduces carbonate alkalinity. This reduction in alkalinity results in CO_2 outgassing when waters equilibrate to surface conditions, and reduces the riverine export of carbon and alkalinity by roughly 33% annually. Future changes in snowmelt dynamics that control the balance of carbonic and sulfuric acid weathering may substantially alter carbon cycling in the East River. Ultimately, we demonstrate that differential C-Q relationships between major solutes can provide unique insights into the complex subsurface flow and biogeochemical dynamics that operate at catchment scales.

1 Introduction

The storage of water as winter snowpack followed by release as snowmelt represents an important natural source of freshwater for large portions of the globe. As snowmelt moves through the subsurface, it accumulates solutes through chemical weathering reactions and the breakdown of organic matter. The generation and export of these solutes, as well as the mixing of flow paths that experience differential reaction networks and progress, exert a direct control on water quality [*Todd et al.*, 2012] and the transport of contaminant metals [*McClain and Maher*, 2016; *Nordstrom and Ball*, 1986]. Stream solutes also serve as important fluxes in the global carbon cycle in terms of both the transport of carbon from the terrestrial to the ocean-atmosphere reservoirs [*Bluth and Kump*, 1994; *Galy et al.*, 2007; *Maher and Chamberlain*, 2014; *Raymond et al.*, 2008] and the long-term drawdown of atmospheric CO_2via silicate weathering reactions [*Beaulieu et al.*, 2012; *Berner*, 1991; *Gibbs et al.*, 1999; *Torres et al.*, 2015; *West*, 2012; *Caves et al.*, 2016]. Despite its importance, the subsurface transport and transformation of carbon remain the least understood component of the terrestrial carbon cycle. In the context of modern climate change, understanding the role of snowmelt in solute generation is particularly pressing due to the sensitivity of snowpack to both the direct [e.g., temperature and precipitation: *Jacobs*, 2011; IPCC; *Vano et al.*, 2012; *Lukas et al.*, 2014; *Clow*, 2010; *Mankin et al.*, 2015; *Mountain Research Initiative*, 2015] and indirect [e.g., bark-beetle infestations and forest fires: *Edburg et al.*, 2012; *Bearup et al.*, 2014] consequences of global warming. In this study, we characterize the dynamics of solute generation in a snowmelt-dominated, high-elevation watershed in the central Rocky Mountains through observed concentration-discharge (C-Q) relationships.

As integrators of upstream processes, C-Q relationships provide unique information on the interactions between hydrologic processes and solute generation at large spatial scales. Base cation (Ca^{2+}, Mg^{2+}, Na^{+}, K^{+}) and Si concentrations, which are controlled primarily by chemical weathering reactions (although K^{+} may be biologically cycled), are broadly observed to decrease with increasing discharge. This behavior is thought to reflect the mixing of end-member water sources, such as diluted event waters that have experienced little or no subsurface chemical

reactions and chemically evolved pre-event waters [e.g., *Chanat et al.*, 2002]. However, the wide-spread observation of chemostatic behavior, which is defined by constant or slightly decreasing concentrations with increasing discharge, implies chemical weathering rates and solute fluxes that scale with discharge, seemingly at odds with end-member mixing scenarios [*Hornberger et al.*, 2001; *Scanlon et al.*, 2001; *Godsey et al.*, 2009].

The dynamics of C-Q relationships have also been quantified by considering the balance between water transit time through the subsurface and the rates of chemical reactions [*Hornberger et al.*, 2001; *Maher*, 2010, 2011; *Maher and Chamberlain*, 2014; *Benettin et al.*, 2015; *Ibarra et al.*, 2016]. This framework allows for chemostatic behavior and increasing solute fluxes with increasing discharge. As a result, C-Q relationships at a given location are expected to be highly dependent on temporally nonstationary transit time distributions of water through the subsurface [*Heidbuchel et al.*, 2012; *Harman*, 2014; *Benettin et al.*, 2015], as well as the kinetic and thermodynamic constraints associated with different lithologies [*Bluth and Kump*, 1994; *Ibarra et al.*, 2016], the availability of fresh mineral surface areas with depth [*West*, 2012; *Maher and Chamberlain*, 2014], and reactive gases in the unsaturated zone [*Beaulieu et al.*, 2010; *Berner*, 1992; *Maher et al.*, 2009; *Lawrence et al.*, 2014; *Kim et al.*, 2014].

A relatively unexplored control on C-Q relationships is the presence of vertical chemical gradients, or nested reaction fronts, in the subsurface and their interactions with flow regime. Infiltration of water and subsequent weathering reactions result in vertical chemical gradients in regolith, and due to differing reaction kinetics and thermodynamic limits, these chemical gradients may be offset, as observed recently between carbonate weathering and pyrite oxidation fronts in the Shale Hills Critical Zone Observatory [*Brantley et al.*, 2013]. Changes in water table height, directly related to discharge, may then alter the percentage of flow paths that intersect these different reaction fronts during vertical infiltration, before lateral transport to surface water [*Engdahl and Maxwell*, 2015], thereby providing a direct control on solute C-Q relationships. Herein, we demonstrate the importance of nested reaction fronts within the East River watershed in driving the balance of carbonate weathering by carbonic acid relative to sulfuric acid between the snowmelt and base flow regimes.

Carbonate weathering is controlled by acid-base reactions, primarily via carbonic acid generated by soil respiration. The reaction of CO_2 with calcite ($CaCO_3$(s)) can be represented by:

$$CaCO_3(s) + CO_2(aq) + H_2O \longleftrightarrow Ca^{2+} + 2HCO_3^- \quad (1)$$

A number of studies have also shown the importance of sulfuric acid weathering of carbonates due to pyrite oxidation, particularly in shale-dominated basins [*Galy and France-Lanord*, 1999; *Calmels et al*., 2007; *Li et al*., 2008; *Das et al*., 2012; *Brantley et al*., 2013; *Torres et al*., 2015], described as,

$$2CaCO_3(s) + H_2SO_4 \longleftrightarrow 2Ca^{2+} + 2HCO_3^- + SO_4^{2-} \quad (2)$$

Rates of sulfuric acid weathering are then controlled by the oxidation of pyrite. Due to the relatively rapid kinetics of sulfide oxidation [*Williamson and Rimstidt*, 1994], pyrite oxidation generally occurs deep in the subsurface and has been shown to be highly dependent on water table height [*Todd et al*., 2012; *Manning et al*., 2013; *Brantley et al*., 2013] due to slow diffusion rates of molecular O_2 through water compared to unsaturated soil [*Feng et al*., 2002]. As such, some studies suggest that sulfuric acid weathering rates are extremely sensitive to changing climate and the associated changes in water table height [*Mast et al*., 2010; *Todd et al*., 2012; *Manning et al*., 2013]. Despite its importance to water quality, global carbon and oxygen cycles [*Calmels et al*., 2007; *Torres et al*., 2014], and regolith formation [*Rempe and Dietrich*, 2014], no previous studies to our knowledge have examined intra-annual variability of sulfide oxidation rates and their relationship to discharge.

In contrast to weathering-derived solutes, dissolved organic carbon (DOC) concentrations are generally observed to have a positive correlation with discharge in snow-dominated systems [*Hornberger et al*., 1994]. In the case of DOC, solute production is less directly coupled to fluid flow; instead the production and mineralization of DOC in soil waters is controlled by biological processes such as litter accumulation [*Cotrufo et al*., 2015], enzymatic depolymerization [e.g., *Conant et al*., 2011], and heterotrophic respiration [*Grieve*, 1991]. Catchment C-Q relationships for DOC are then thought to reflect the flushing of high-DOC waters in the upper soil horizons during high runoff events through the activation of hillslopes in runoff generation [*Hornberger et al*., 1994; *Boyer et al*., 1996; *Boyer et al*., 1997; *McGlynn and McDonnell*, 2003; *Perdrial et al*., 2014].

Finally, hysteresis behavior has been observed in both base cation and DOC C-Q relationships, primarily during storm events. Hysteresis behavior describes the directional dependence of solute concentrations at a given discharge and results in different values on the rising versus falling limbs of the hydrograph. *Evans and Davies* [1998] proposed a framework whereby the shape and direction of hysteresis loops allow for the determination of rank-order concentrations of event-, soil-, and groundwater end-members. However, *Chanat et al*. [2002] showed that assumptions of relative volume and timing of the end-member contributions that allow for unique hysteresis

characteristics with a given concentration rank-order are often violated in natural settings as a result of storm intensity and antecedent moisture conditions. Further, assumptions of constant end-member concentrations cannot account for transitions between chemostatic and dilution behavior that are observed in some streams above a given threshold discharge [*Maher*, 2011].

In this paper, we compare C-Q relationships and hysteresis patterns between weathering-derived base cations, anions, DIC and DOC in the East River Watershed near Gothic, CO. As these solutes reflect differential formation processes, we argue that their comparison leads to a more complete conceptual model for the hydrologic controls on solute generation. Specifically, the differential C-Q behavior of cations, anions, DIC, and DOC demonstrates the seasonal evolution of flow regime in relation to vertical chemical gradients in the subsurface, which ultimately impact the ability of the East River to export carbon and alkalinity.

2 Site Description

Our study site is the headwaters of the East River, located near Gothic, Colorado (USA) within the Gunnison River basin. The East River catchment is a mountainous, high-elevation watershed where stream flow is dominated by snowmelt in the spring and summer months and thus broadly representative of similar catchments throughout the Rocky Mountains that supply downstream water [*Markstrom et al*., 2012]. The East River contributes 25% percent of Gunnison River discharge [*Ugland et al*., 1991], which in turn contributes 40% of Colorado River discharge at the Colorado-Utah state line [*Spahr et al*., 1999]. Across the region, total water demand is roughly equal to the native supply [*Colorado Water Conservation Board*, 2002], stressing the importance of snowmelt processes and water quality to human systems.

The data presented herein was collected at and upstream of the Pumphouse locality, located roughly 5 km south of the Rocky Mountain Biological Laboratory (RMBL) and within the Lawrence Berkeley National Laboratory's Watershed Science Focus Area (LBNL SFA) (Figure 1). Upstream catchment area is 85 km^2 with elevations that span 2760–4123 m and an average elevation of 3350 m. The catchment is oriented NW-SE with dominant aspects perpendicular to the orientation (histogram peaks at 63° and 200°), and the terrain is steep with an average slope of 23°. The watershed is composed of three life zones: montane (including spruce and aspen forests and meadows), subalpine, and alpine. Annual average temperature at the site is 1°C, and the area-weighted average precipitation across the basin is 1.23 ± 0.26 m/yr [*PRISM*, 2013] with the majority occurring as snowfall.

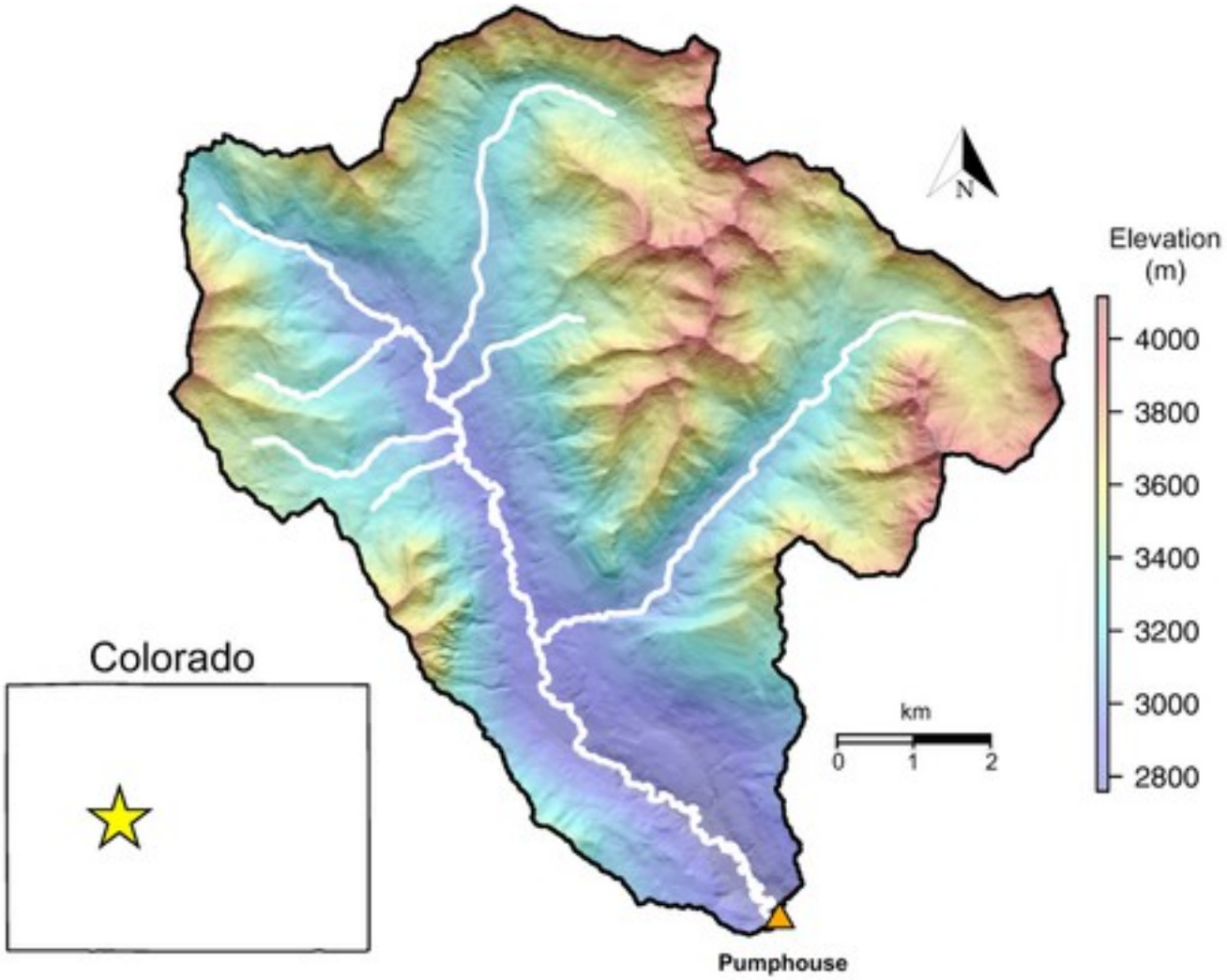

Figure 1
Open in figure viewerPowerPoint
Site location map. East River watershed (85 km^2) with hill-shade and color-coded topography, and Colorado state map with yellow star denoting watershed location. The Pumphouse stream sampling locality is shown as the orange triangle, and East River surface water shown in white.

The catchment is dominated by the Cretaceous Mancos Shale Formation, with carbonate and pyrite contents of roughly 20% and 1%, respectively [*Morrison et al*., 2012], and the spatially variable presence of surficial glacial and alluvial sediments [*Gaskill et al*., 1967, 1991; *Bryant*, 1969; *Mutschler*, 1970]. Broadly, the floodplains and lower slopes are overlain by Quaternary colluvium and alluvium. The upper tributaries of the catchment are underlain by calcareous shale from the Cretaceous Mancos Formation, with outcrops of Tertiary quartz monzonite. The eastern side of the catchment is underlain by a combination of Mancos

shale, Paleozoic sedimentary rocks (Morrison, Maroon, and Gothic Formations), and Tertiary granodiorite.

3 Sampling, Analysis Methodology

3.1 Hydrology: Transducers and Discharge Curves

Instantaneous stream discharge measurements (n = 8) were done at the Pumphouse site (Figure 1) using a SonTek FlowTracker® acoustic Doppler velocimeter at 0.5 m intervals along a 13.5 m cross section. Measured discharge spans 0.58 m^3/s at base flow to 8.6 m^3/s in late June 2015. A power function best describes the depth-discharge rating curve ($r^2 = 0.96$) which relies on a Solinst Levellogger® Edge pressure transducer atmospherically corrected with barometric pressure. Collection of subhourly transducer data began 1 September 2014. Calculated mean daily flow ranges from 0.10 to 14.0 m^3/s. Correlation ($r^2 = 0.97$) of daily flows with the U.S. Geological Survey stream gage East River at Almont (09112500) allowed correction of stream discharge during iced periods in the winter and an extension of back-calculated flow to 1 May 2014 in order to coincide with solute collection.

The hydrograph is dominated by snowmelt across the observation period with lower snowfall in 2015 resulting in lower discharge values compared to 2014. However, both years experience a rising hydrograph in early April and peak discharge is reached in early June. This is followed by a decay to base flow values through the summer and fall (Figure 2a). As shown, monsoonal storm events in August and September result in smaller, transient increases in discharge that decay quickly to pre-event discharge rates.

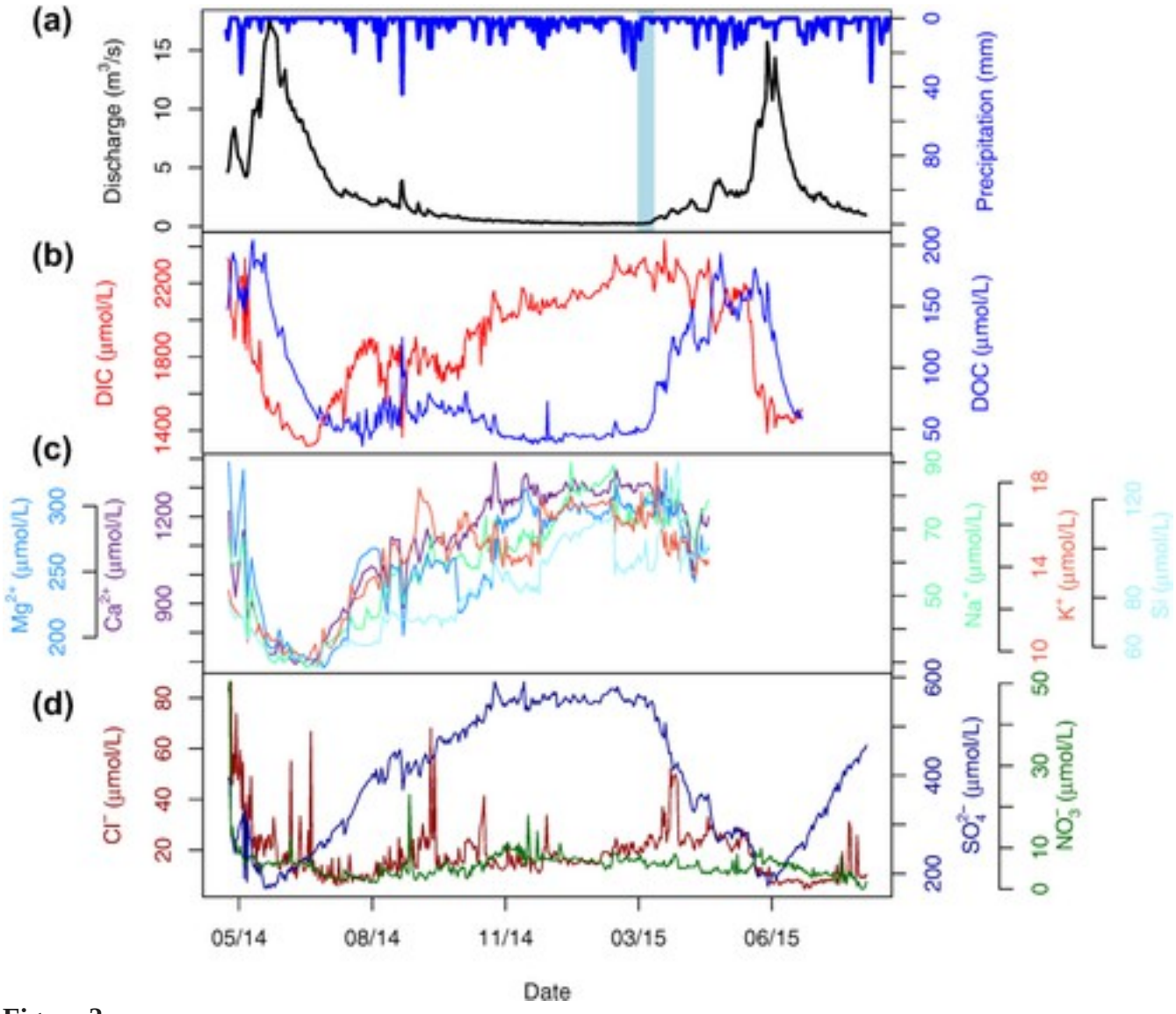

Figure 2

Open in figure viewerPowerPoint

Hydrology and solute concentrations. (a) Discharge rates and daily precipitation amounts. Light blue line denotes the date of peak snowpack. (b) DIC and DOC concentrations. (c) Cation concentrations. (e) Anion concentrations.

3.2 Chemical: Stream Water Sampling, Dissolved Solids Measurements, DOC, NPP

Stream water samples were collected daily from May 2014 to August 2015 using an automatic water sampler (Model 3700; Teledyne ISCO, NE, USA). Samples were pumped via peristaltic pump into uncapped 1 L polyethylene bottles and retrieved at regular intervals. Bulk samples were filtered using 0.45 µm Hydrophilic Polyvinylidene Fluoride (PVDF) syringe filters into

individual vials for subsequent anion, base cation, and dissolved organic and inorganic carbon analysis, as previously described [*Williams et al*., 2011; *Long et al*., 2015]. Briefly, chloride, nitrate, and sulfate concentrations were quantified via ion chromatography, while base cation concentrations were determined using inductively coupled plasma mass spectrometry. Dissolved organic carbon and dissolved inorganic carbon (DIC) concentrations were determined using a TOC-VCPH analyzer (Shimadzu Corporation, Japan). DOC was analyzed as nonpurgeable organic carbon (NPOC) by purging acidified samples with carbon-free air to remove DIC prior to measurement.

Atmospheric deposition rates were taken from the National Atmospheric Deposition Program (NADP) site CO10 located in Gothic, CO (elev. 2915 m) within the East River Pumphouse drainage area [*NADP*, 2016]. Annual deposition rates were averaged over the period 2000–2014 to compare to river concentrations. Precipitation at the NADP site was 0.732 and 0.690 m for water years 2014 and 2015, respectively. In 2014, the fraction of precipitation that fell at this site as snow was 0.66 while whereas in 2015 this fraction dropped slightly to 0.59.

To determine the potential influence of gypsum ($CaSO_4$) dissolution in driving SO_4^{2-} and Ca^{2+}C-Q patterns, we calculate the saturation index (SI) of Pumphouse water samples as,

$$SI = log\left(\frac{IAP}{K_{gypsum}}\right) = log\left(\frac{[Ca^{2+}][SO_4^{2-}]}{2.93\times10^{-5}}\right), \quad (3)$$

where IAP is the ion activity product and K_{gypsum} is the equilibrium constant for gypsum. We use the log(K_{gypsum}) for 0˚C from *Johnson et al*. [1992] and assume that concentrations are equivalent to activities.

To estimate net primary productivity (NPP) in order to compare stream carbon output fluxes to input fluxes, we use MODIS NPP satellite data spanning 2000–2014. The MOD17A3 NPP data product is at 1 km^2 resolution and was retrieved from the online Data Pool, courtesy of the NASA Land Processes Distributed Active Archive Center (LP DAAC), USGS/Earth Resources Observation and Science (EROS) Center, Sioux Falls, South Dakota, https://lpdaac.usgs.gov/data_access/data_pool. We calculate an NPP average from 2000 to 2014 within the catchment area upstream from the Pumphouse collection locality of 236.3 ± 104.4 tC/km^2/yr where errors are calculated as the standard deviation of annual NPP from grid cells within the catchment area.

4 Results

4.1 Base Cations and Anions

Dissolved solid fluxes are dominated by Ca^{2+} and Mg^{2+}, with smaller contributions from SiO_2, Na^+, and K^+, characteristic of carbonate-dominated weathering fluxes (Table 1). Base cation concentration ranges are 679–1388 µM for Ca^{2+}, 177–334 µM for Mg^{2+}, 51–135 µM for Si, 28–90 µM for Na^+, and 9.2–19 µM for K^+. The lowest concentrations occur during peak snowmelt discharge and highest concentrations occur during the winter base flow periods (Figure 2c). Despite the two orders of magnitude ranges in base cation concentrations, base cations all display similar and moderately chemostatic behavior across the range of observed discharge. This is shown in Figure 3d, where concentrations decrease by a factor of 0.5, except Na^+, which decreases by a factor of 0.66, while discharge increases by a factor of 20. Atmospheric deposition accounts for <1% of observed concentrations for Ca^{2+} and $Mg^{2+}$and 5% of observed concentrations for K^+ and Na^+ (Table 1).

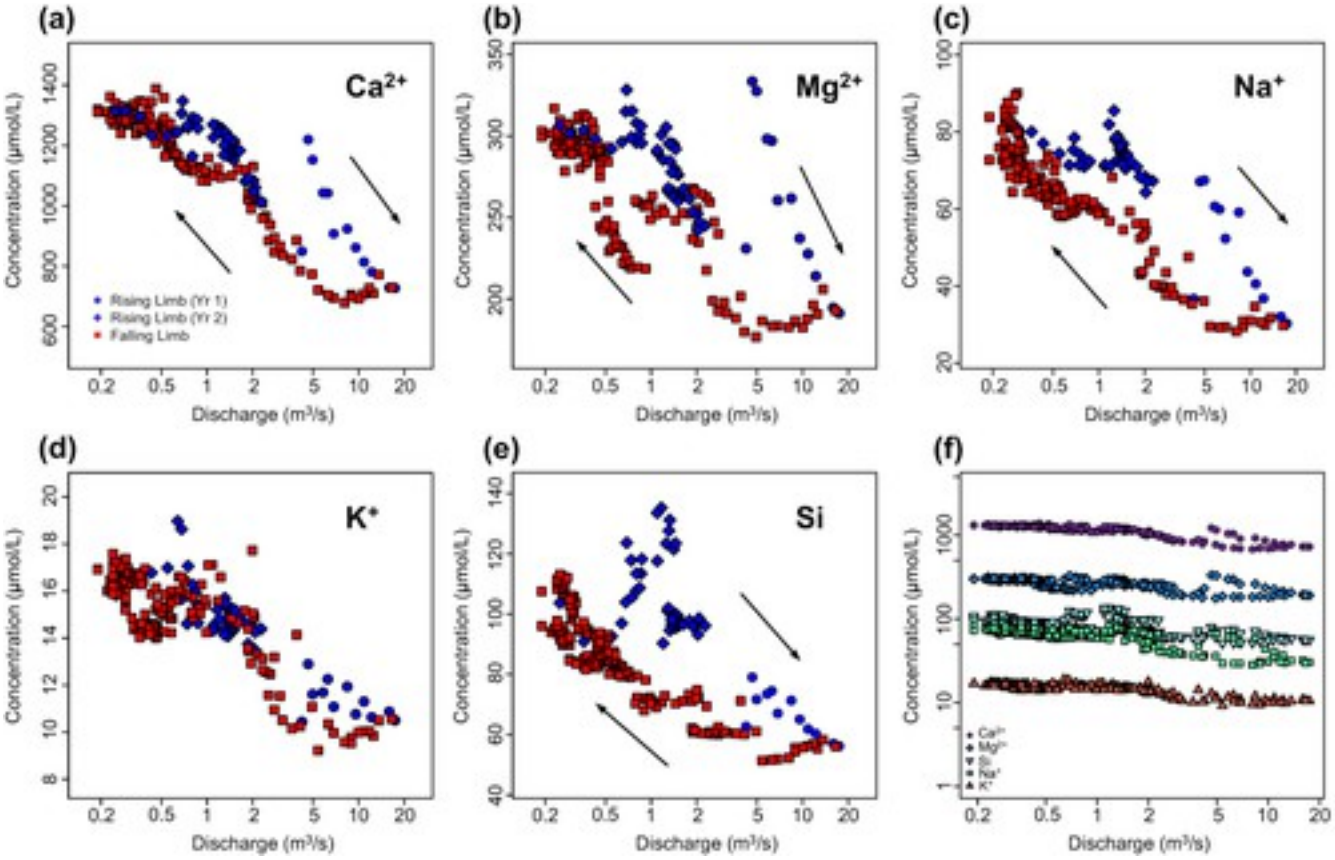

Figure 3

Open in figure viewerPowerPoint

Dissolved solid C-Q relationships. (a–e) semi-log Ca^{2+}, Mg^{2+}, Na^+, K^+, and Si to show annual hysteresis patterns. Blue points represent the rising limb of the hydrograph, and red points represent the falling limb, and first year and second year rising limbs are denoted by shape. (f) Log-log C-Q for all base cations and Si demonstrating relative concentrations and consistent chemostatic behavior.

Table 1. Concentration Data

	Concentration (μmol/L)			
	Average	**Maximum**	**Minimum**	**Atmospheric Deposition[a]**
DIC	1917.2	2434.2	1314.8	
DOC	86.4	204	36.1	
Ca^{2+}	1167	1388	679	4.7
Mg^{2+}	269	334	177	0.66
Na^{+}	64.4	90	28	1.5
K^{+}	14.8	19	9.2	0.54
Si	87.3	135	51	
SO_4^{2-}	385.7	591.3	169.3	3.38
Cl^{-}	21.1	854.1	4.8	1.49
NO_3^{-}	5.78	50.4	0.1	10.1

	Concentration (µmol/L)			
	Average	Maximum	Minimum	Atmospheric Depositiona
Cation equivalentb	2951	3452	1760	
Cation Eq. −2*[SO_4^{2-}]	2024	2431	1309	

- a Data from *NADP* [2016].
- b 2*[Ca^{2+}] + 2*[Mg^{2+}] + [Na^{+}] + [K^{+}].

Additionally, base cation C-Q patterns display coherent negative, clockwise hysteresis with higher concentrations on the rising limbs than the falling limbs of the hydrograph. These hysteresis patterns are shown by semi-log plots of C-Q in Figures 3a–2e. Rising limb behavior is varied across base cations: $Ca^{2+}$and Mg^{2+} both display dilution at lower discharges in the second year; K^{+} concentrations show consistent dilution with increasing discharge across the 2 years and only weak hysteresis; and Si displays small increases in concentration at the start of the rising limb followed by dilution. All base cations appear to show a two-stage return to maximum base flow concentrations on the falling limb, while Si displays discontinuous step-wise behavior. We note that assuming power-law behavior and plotting C-Q relationships in log-log space obscures hysteresis patterns and coherent dilution trends (Figure 3f), and therefore we do not use the slope of log-log relationships [e.g., *Godsey et al*., 2009; *Stallard and Murphy*, 2014] to analyze C-Q behavior.

Major anion C-Q relationships, including SO_4^{2-}, Cl^{-}, and NO_3^{-}, are shown in Figure 4. Sulfate dominates dissolved anion fluxes with concentrations ranging from 170 to 590 µM. In contrast to base cations, SO_4^{2-} displays no significant hysteresis pattern; concentrations are constant to 0.5 m^3/s discharge, above which dilution occurs. Additionally, SO_4^{2-} dilution occurs earlier than DIC and base cation dilution (Figure 2). Though dilution of SO_4^{2-} is stronger than for base cations, SO_4^{2-} fluxes still increase with increasing discharge. Nitrate concentrations range from 1 to 50 µM but largely fall between 2 and 10 µM, and Cl^{-} concentrations range from 4 to 850 µM but largely fall between 2 and 20 µM. Both Cl^{-} and NO_3^{-} concentrations appear to display path-

dependent behavior, although the large variability between the 2 years of observations limits its interpretation. In particular, NO_3^- concentrations do not rise significantly during the second year of snowmelt despite markedly high levels during snowmelt the first year and transient increases with monsoonal storms (Figure 2d), which may relate to changes in snowmelt characteristics (rate, integrated amount) as well as in-stream processing. Atmospheric deposition accounts for 1.7% of observed SO_4^{2-}, 500% of NO_3^-, and 25% of Cl^- minimum concentrations.

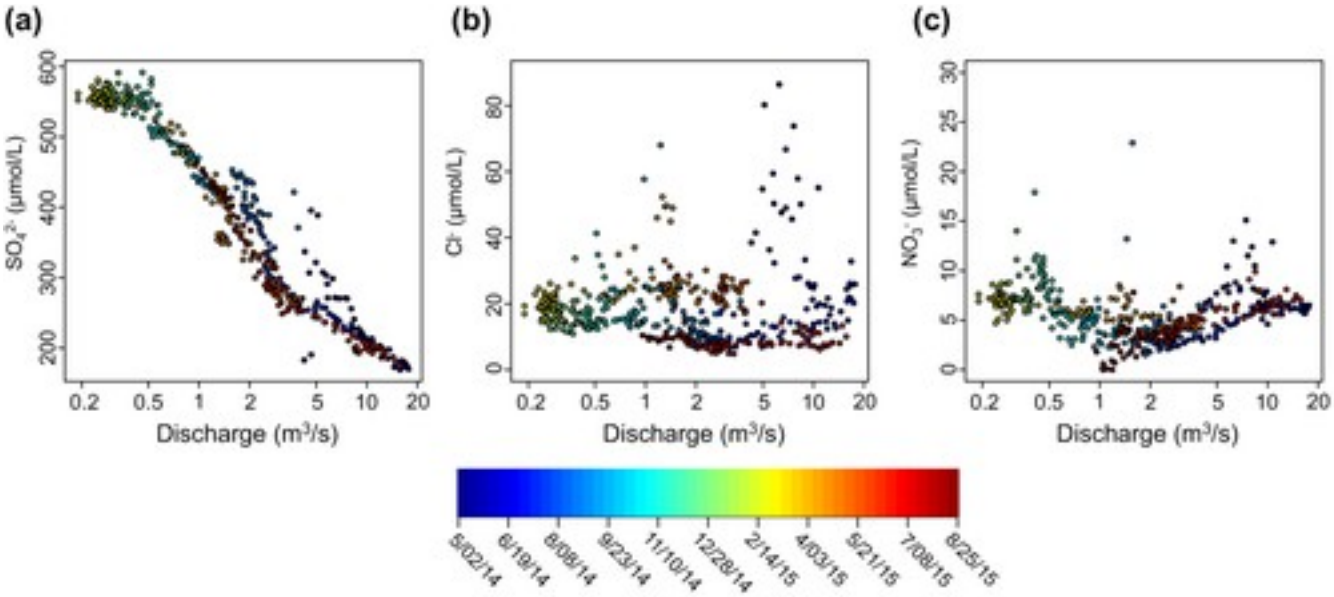

Figure 4
Open in figure viewerPowerPoint
Anion C-Q. (a) Sulfate; (b) chloride; and (c) nitrate, all color-coded by date.

4.2 Carbon

4.2.1 DOC

Concentrations of DOC at the Pumphouse locality range from 36.1 to 204 μM over the measurement period with a positive, hysteretic correlation with discharge as shown in Figure 5a. Temporally, DOC concentrations increase rapidly on the rising limb of the hydrograph during the initial spring snowmelt and reach peak values before peak discharge in both years of observation (Figure 2b). Concentrations begin to decrease when discharge reaches roughly 7 m^3/s, and continue to decrease on the falling limb of the hydrograph at lower concentrations than on the rising limb. Concentrations reach minimum values at a discharge of 2.0 m^3/s, rise slightly as discharge decreases to 1.0 m^3/s, and return to minimum values at 0.5 m^3/s. The result of this temporal path is a coherent clockwise hysteresis pattern, similar to that observed for DOC during snowmelt in numerous catchments [*Hornberger et al.*, 1994]. Storm event hysteresis is also

observed superimposed over the annual pattern during the summer monsoon months. Interestingly, however, the hysteresis pattern is counter-clockwise for the largest observed storm event with lower DOC concentrations on the rising limb than on the falling limb from 7 to 14 September 2014, as highlighted in Figure 5a.

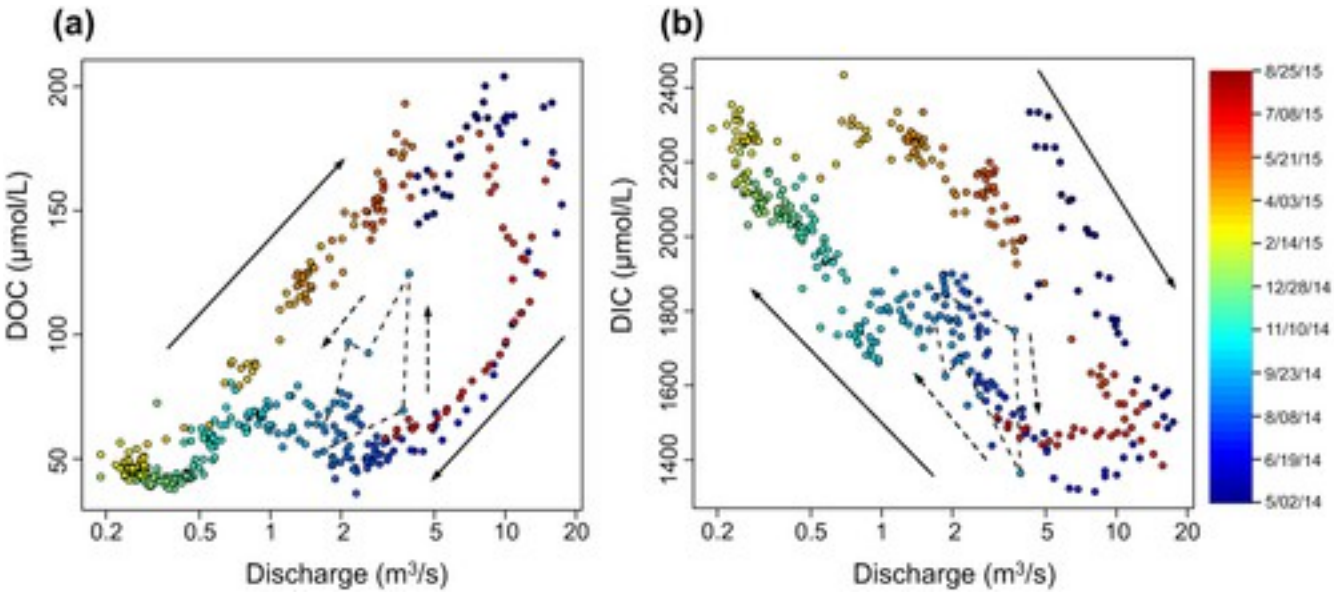

Figure 5

Open in figure viewerPowerPoint

Carbon C-Q. (a) DOC C-Q and (b) DIC C-Q, both color-coded by date with cation equivalent and cation equivalent corrected for sulfate. Both plots show storm hysteresis as well for the 7–14 September 2014 event represented by dashed arrows.

Though comparative data are limited due to the temporal span of observations, we observe differential characteristics of C-Q behavior between the two snowmelt periods where data extend into the second snowmelt period. During the second year over which observations cover the snowmelt period, concentrations rise to higher values at lower discharge compared to the first year observations, with maximum concentrations observed at discharges of 3 and 10 m^3/s in the second and first years, respectively. DOC concentrations then decrease more sharply in the second year at discharges above 7 m^3/s. Below discharges of 10 m^3/s on the falling limb, concentrations are remarkably consistent between the 2 years of observation.

Annual observed DOC fluxes are 1.097 ± 0.155 $tC/yr/km^2$, falling between globally observed values for mixed northern forests (0.9–12.35 $tC/yr/km^2$) and cool grasslands (0.1–0.95 $tC/yr/km^2$) [*Aitkenhead and McDowell*, 2000], likely reflecting the spectrum of East River vegetation. Due to the positive correlation between DOC concentration and discharge, annual fluxes are dominated by periods of high discharge to a greater extent than DIC, cations, and anions, with

roughly 20% of the total annual flux occurring in the 10 days of highest flow and 50% in the month of highest flow. In comparison to MODIS satellite data, riverine DOC fluxes represent 0.5% of annual NPP in the upper East River, similar to global flux balances.

4.2.2 DIC and Cation-Equivalent

Concentrations of dissolved inorganic carbon (DIC) in the East River at Pumphouse range between 1314.8 and 2434.2 μM with a negative, hysteretic relationship with discharge (Figure 5b). As pH observations range from 8.1 to 8.6, the majority of DIC occurs in the form of HCO_3^- with additional contributions from CO_3^{2-} and CO_2(aq). During snowmelt, DIC concentrations appear relatively constant to 2 m^3/s discharge in the second year and potentially up to 5 m^3/yr in the first year, although lack of observational data for the initial first year rising limb precludes a precise analysis. Concentrations then decrease with increasing discharge with minimum DIC occurring at peak discharge in the second year and on the falling limb at 7 m^3/s in the first year. The return to maximum concentrations at base flow appears to be a two-step process with constant or slightly decreasing values from 2 to 1 m^3/s interrupting the general increase. This step coincides with increases in DOC as mentioned in the previous section. Also shown in Figure 5b is the 7–14 September 2014 storm event, which displays clockwise hysteresis similar to the annual C-Q pattern. The result of clockwise DIC hysteresis and counter-clockwise DOC hysteresis is a strong negative correlation between DIC and DOC concentrations during the storm event (Figure 2b).

The negative, clock-wise hysteresis pattern matches the general base cation patterns, particularly for $Ca^{2+}$and Mg^{2+}, which dominate dissolved solid fluxes. Assuming chemical weathering occurs fully through acid-base reactions between carbonic acid and rock, cation equivalent represents the carbonate alkalinity expected in solution from weathering reactions (HCO_3^-). As shown in Table 1, there are large discrepancies between DIC and cation equivalent ranging from 321.8 to 1183 μM. This DIC-cation equivalent discrepancy is due to the large contributions of sulfuric acid to weathering fluxes as will be discussed in section 5.2. Despite these discrepancies, the similarity in hysteresis patterns shows that DIC exports are dominated by chemical weathering reactions.

Similar to DOC, DIC C-Q relationships display some variability between the 2 years of observations. Specifically, dilution is stronger and occurs at a lower discharge in the second year relative to the first year. Additionally, concentrations reach minimum values at peak discharge in the second year, whereas dilution continues into the falling limb in the first year. Annual DIC fluxes are 17.165 tC/yr/km^2—roughly 16 times greater than DOC fluxes. Due to the role of

sulfuric acid weathering, a comparison of DIC fluxes to NPP and examination of the role of heterotrophic respiration in DIC exports is discussed in section 5.3.

5 Discussion

In this section, we discuss the dominant chemical weathering regimes and seasonal dynamics of weathering fluxes inferred from differential C-Q relationships between major solutes. First, we demonstrate that dissolved solid fluxes are dominated by the dissolution of calcite in the Mancos shale based on the relative concentrations of base cations. Next, we evaluate the role of sulfuric acid derived from pyrite oxidation in driving calcite dissolution and compare calculated pyrite oxidation rates with previously published results from shale-dominated catchments across the globe. Finally, we present an overview of the differential C-Q relationships observed across major solutes. As vertical gradients of DOC, calcite, and pyrite in the subsurface are expected to be offset or nested in a predictable manner, differential C-Q relationships reveal seasonal changes in the intersection of subsurface flow paths with these nested reaction fronts.

5.1 Carbonate Versus Silicate Weathering

To characterize the relative weathering contributions of carbonates and silicates to dissolved solid exports, we follow the methods of *Gaillardet et al*. [1999] and evaluate Na^+-normalized concentrations of Ca^{2+} and Mg^{2+}, as shown in Figure 6. Waters that drain carbonate-dominated basins show higher Ca/Na and Mg/Na ratios (roughly 50 and 10, respectively) than silicate-dominated basins (roughly 0.35 and 0.24, respectively) due to higher ratios in the host rock [*Gaillardet et al*., 1999]. Relative contributions to dissolved fluxes can then be inferred by a mixing model between global end-member ratios of carbonate-dominated and silicate-dominated streams. This is shown in Figure 6, where Mg/Na are plotted against Ca/Na values for Pumphouse measurements and compared to carbonate and silicate end-member stream concentrations. Pumphouse values overlap carbonate end-member values, suggesting that carbonate weathering dominates dissolved solid fluxes in the East River. Additionally, modeling of groundwater solutes using regional Mancos Shale chemical composition suggests that Na^+ concentrations may become elevated due to cation exchange with clay [*Morrison et al*., 2012]. This would cause an underestimation of carbonate weathering contributions based on the methods of *Gaillardet et al*. [1999]. Taken together, we estimate 75–100% carbonate weathering based on Pumphouse values as a rough range.

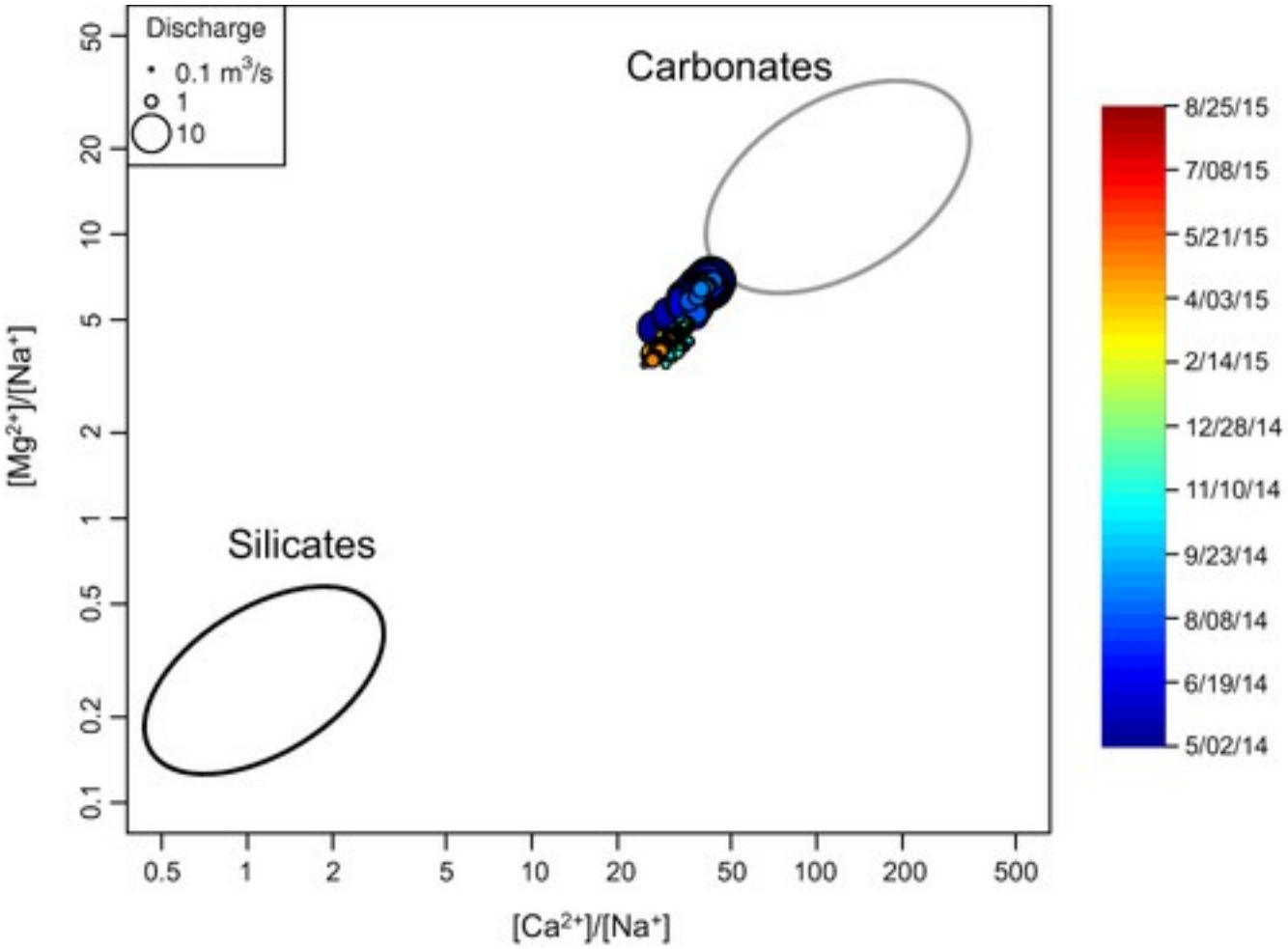

Figure 6

Open in figure viewerPowerPoint

Carbonate versus silicate weathering. Base cation ratios of Pumphouse waters compared on *Gaillardet et al*. [1999] mixing model for Ca/Na versus Mg/Na of carbonate and silicate end-member catchment ratios. Points are color-coded by date and sized by discharge.

5.2 Proportions of Carbonic and Sulfuric Acid Weathering

The relative contributions of carbonic and sulfuric acids to East River weathering rates are examined using mixing models of stoichiometric balance for each given reaction, following the methods of *Li et al*. [2008]. Carbonic acid weathering of carbonate rock generates 2 moles of HCO_3^- for every mole of Ca^{2+} or Mg^{2+}, whereas sulfuric acid weathering of carbonate rock generates 1 mole of HCO_3^- for every mole of $Ca^{2+}$and Mg^{2+}, with the remaining charge imbalance accounted for by 0.5 moles of SO_4^{2-}. Assuming carbonate rock weathering dominates dissolved solid fluxes, the proportions of carbonic and sulfuric acid weathering are then calculated using a carbonic acid end-member value (HCO_3/(Ca + Mg) = 2; SO_4/(Ca + Mg) = 0) and a sulfuric acid end-member value (HCO_3/(Ca + Mg) = 1; SO_4/(Ca + Mg) = 0.5), as shown in Figure 7a.

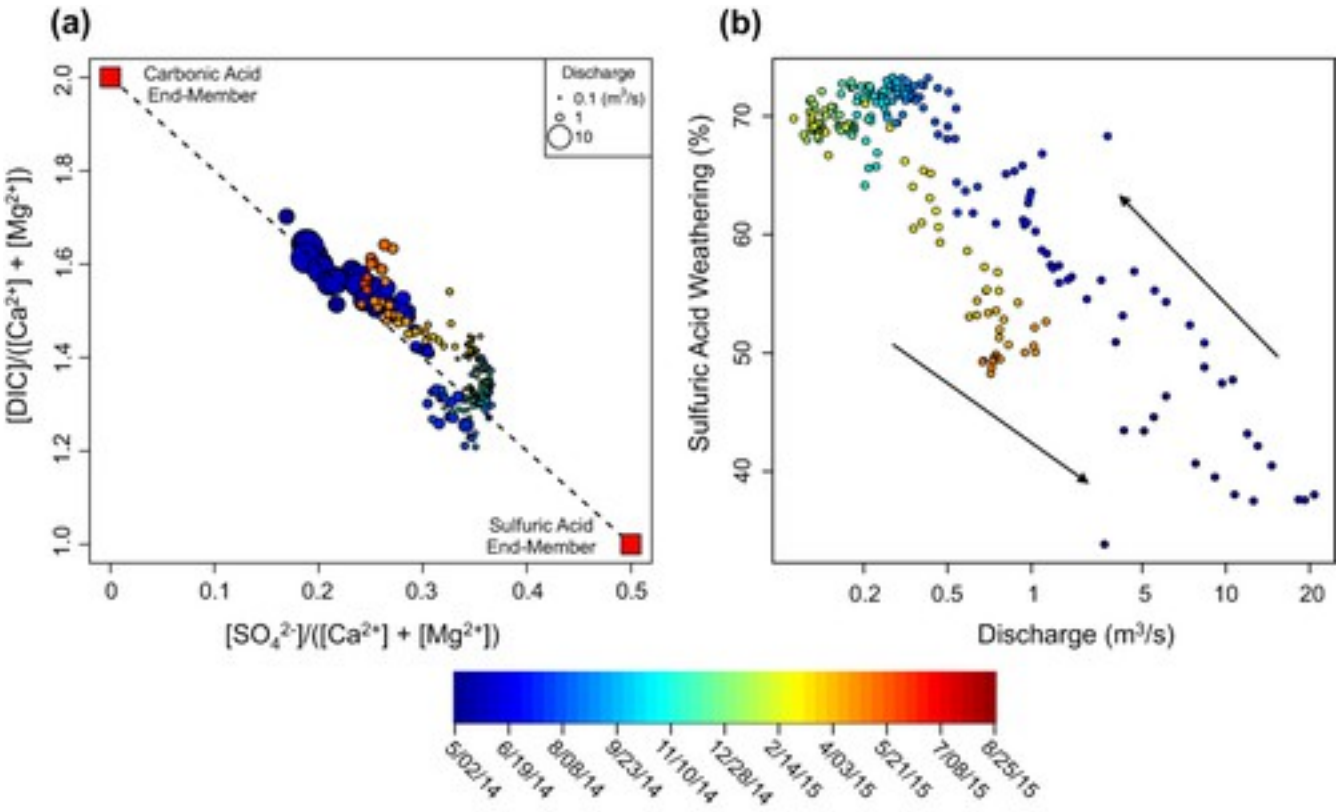

Figure 7
Open in figure viewerPowerPoint

Carbonic acid versus sulfuric acid weathering. (a) Carbonic acid versus sulfuric acid end-member mixing model with points color-coded by date and sized by discharge. End-members based on stoichiometry in equations (1) and (2). (b) Sulfate weathering percentage showing a high dependence on discharge along with annual counterclock-wise hysteresis.

Sulfuric acid weathering accounts for 35–75% of carbonate dissolution throughout the year, with a strong dependence on discharge (Figure 7b). Sulfuric acid contributions are highest at low discharge and lowest at high discharge. Additionally, there is a degree of hysteresis, with a lesser contribution from sulfuric acid on the rising limb of the hydrograph compared to the falling limb. The flux-weighted average of sulfuric acid weathering accounts for 52% of $Ca^{2+}$and Mg^{2+} fluxes due to dominance of snowmelt on total discharge and dissolved fluxes. When sulfate anion equivalents (2* SO_4^{2-}) are subtracted from cation-equivalent concentrations to account for sulfuric acid weathering (equation 2), these corrected cation-equivalent values roughly match measured DIC concentrations. Corrected cation-equivalent concentrations are slightly lower than DIC concentrations by an average of 63 μmol/L (Table 1), which is likely due to the presence of atmosphere-equilibrated CO_2(aq) in samples. This creates a small discrepancy between measured

DIC concentrations, which include CO_2(aq), and carbonate alkalinity concentrations, which should balance cation-equivalent concentrations.

Although the secondary precipitation of gypsum in Mancos shale in semi-arid groundwater basins has been noted due to high rates of sulfide oxidation and carbonate weathering, gypsum is not expected to be present as a primary phase in the Mancos shale at our field site. Calculated SI of gypsum range from −4.2 at low discharge to −6.0 at high discharge showing that waters are extremely under-saturated with respect to gypsum. If mineral availability is not limiting gypsum dissolution, we would expect much higher values of gypsum saturation. If instead gypsum only occurred at greater depths so that dilution represented decreasing contributions from deep waters, the observation of chemostatic behavior at discharge below 0.5 m^3/s would also be inconsistent with gypsum dissolution at such high degrees of under-saturation. Specifically, because waters are highly under-saturated with respect to gypsum, dissolution rates should be a function of subsurface transit times for infiltrating waters and available mineral surface area. If sulfate concentrations were controlled by gypsum dissolution and ultimately by transit time, we would expect to see consistent dilution over the range of observed discharge. Thus, due to the absence of gypsum as a primary phase and based on the C-Q behavior of sulfate, we preclude gypsum dissolution as a significant source of sulfate in the upper East River.

In terms of atmospheric deposition, SO_4^{2-} concentrations in regional precipitation are two orders of magnitude less than stream concentrations; we therefore neglect atmospheric deposition in our calculations of sulfide oxidation rates. Assuming all of sulfate in the East River then comes from pyrite, pyrite oxidation-derived fluxes of sulfate are $2.75 \times 10^5 mol/km^2/yr$. This rate is 3–4 times higher than measured rates in the Mackenzie River basin (7.3×10^4 $mol/km^2/yr$) [*Calmels et al*., 2007] and the Ganges-Brahmaputra ($7.9 \times 10^4 mol/km^2/yr$) [*Galy and France-Lanord*, 1999] potentially due to the smaller size of the upper East River catchment, increased proportion of shale in the subsurface, and the local mineralogy, though the East River values are an order of magnitude less than rates from the Kaoping basin in Taiwan (2.4×10^6 $mol/km^2/yr$) [*Das et al*., 2012]. These high rates of pyrite oxidation and surface area-outsized contributions to estimated global fluxes (100 times more percentage contribution to global oxidized sulfide flux than to global land area) add support to the growing body of evidence that global pyrite oxidation fluxes are likely higher than previous estimates [*Berner and Berner*, 1996; *Calmels et al*., 2007; *Torres et al*., 2014].

5.3 Differential C-Q Dynamics

As described above, C-Q relationships for dissolved solids vary widely in both the direction of correlation and hysteresis characteristics. This is caused by a combination of differences between solute generation processes—driven by acid-base, oxidation-reduction, and biological factors—and the location of these processes within the subsurface relative to subsurface flow pathways. In evaluating the observed trends, these solutes can be thought of as tracers of flow depth in the subsurface. As weathering fronts develop, pyrite oxidation tends to occur deepest in the subsurface and may initiate the formation of saprolite and regolith via the acidification of deep pore-waters and subsequent increases in bedrock porosity [*Brantley et al*., 2013]. Trace metals may be mobilized by pyrite oxidation, but retained via sorption onto secondary minerals. Carbonate dissolution may then occur in two reaction fronts—one at or below the pyrite oxidation front due to H_2SO_4 from pyrite oxidation, and at shallower depths due to neutralization of H_2CO_3(aq) from below-ground respiration. Organic carbon buildup occurs in the shallowest subsurface, with DOC concentrations in soil water decreasing exponentially with depth. Comparing these differential C-Q patterns then offers unique insights into subsurface flow paths that may experience different chemical conditions as a function of how they intersect vertical chemical gradients. C-Q patterns of DOC within the East River display year-to-year variability on the rising limb, robust hysteresis with lower concentrations for a given discharge combined with remarkably similar year-to-year concentrations on the falling limb. As demonstrated by previous studies, the behavior of DOC generally reflects the activation of shallow subsurface environments, particularly along hillslopes, during the generation of runoff [*Hornberger et al*., 1994; *Boyer et al*., 1996; *McGlynn and McDonnell*, 2003]. In this conceptual model, soluble organic matter builds up in the shallow subsurface as plant litter is broken down via enzymatic depolymerization and is depleted via microbial respiration. As such, mineralization of organic matter works in competition with dissolved organic carbon exports. On a global scale for example, C:N ratios in soils, which serve as a metric of substrate quality and the ability of microbes to respire carbon, is a robust predictor of DOC fluxes by different biomes. Biomes with unfavorable oxidation conditions that exhibit high C:N ratios, such as in swamps and peatlands, generally have higher DOC stream fluxes [*Aitkenhead and McDowell*, 2000]. East River DOC concentrations begin to rise immediately with the initiation of snowmelt in the spring, reflecting the movement of melt-water through the upper soil horizons and the mobilization of residual high-DOC waters in the upper soil horizons. We postulate that during this period, microbial respiration does not compete with flushing due to low snowmelt temperatures, saturated conditions that inhibit O_2 availability, and the rate of flushing.

On a storm event scale, hysteresis in DOC is thought to reflect changing contributions from surface versus groundwater [*Mei et al*., 2014]. In contrast, the hysteresis observed over seasonal

timescales during snowmelt instead reflects the depletion of soluble carbon from the upper soil horizon during the initial stages of snowmelt [*Hornberger et al*., 1994; *Boyer et al*., 1996]. Progressive infiltration of snowmelt will then pick up progressively less organic carbon. In other words, the new water or soil water end-member value evolves over time due to depletion of available solute. In addition to the observation that peak DOC concentrations occur before peak discharge values in both years of observation, this depletion of soluble carbon is also supported by the change in hysteresis direction in the observed storm event (counter-clockwise) compared to snowmelt (clockwise). During the storm event, initial increases in runoff are sustained by groundwater contributions resulting in steady DOC concentrations, followed by contributions of high-DOC shallow flow path waters. This represents a lag between the transit of new, shallow-flow path waters and the increase in discharge following the storm event, which may in part be due to flood wave duration and the antiphasing of stream stage and water table depths [*Mei et al*., 2014].

This same lag may be present during the initiation of snowmelt, but if so, is immediately overwhelmed by the prolonged infiltration of snowmelt and depletion of upper soil horizon DOC before returning to base flow discharge. Differences in year-to-year characteristics are likely related to a combination of variability in primary productivity and soil DOC buildup from the previous year, along with timing, duration, and magnitude of snowmelt. Year-to-year similarities between DOC concentrations on the falling limbs have a number of potential causes including consistency in upper-soil DOC concentrations after the initial flushing, similar discharge contributions from shallow subsurface flow paths on the falling limb regardless of snowmelt timing or magnitude, and/or similar timescales for the return to base flow after reaching peak discharge.

The differential C-Q dynamics of sulfate, base cations, trace metals, and DIC, in contrast, reveal the complex interplay between carbonic and sulfuric acid weathering of carbonate in the subsurface. As mentioned above, studies of elemental concentrations in weathering profiles show that pyrite oxidation tends to occur deep in soils, largely controlled by water table depth. As such, sulfate concentrations can provide insights into deep subsurface flow paths that reach the pyrite oxidation front during vertical infiltration. Described above, concentrations are stable to a discharge of roughly 0.5 m^3/s after which they are diluted, though sulfate fluxes and associated pyrite oxidation rates still increase over the range of observed discharge. This behavior suggests that the contribution of deeper flow paths plays a decreasing role with increasing discharge during snowmelt, which is consistent with DOC patterns described above. This decreasing contribution may represent a combination of (1) reduced contributions from groundwater with a

consistent end-member concentration and (2) decreased pyrite oxidation rates as the water table rises and inhibits O_2 diffusion across the pyrite oxidation front. In either case, the earlier and stronger dilution of sulfate concentrations relative to DIC (Figure 2) is consistent with pyrite oxidation occurring deep within the weathering profile and with increasing DOC concentrations that imply a shift from deep to shallow subsurface flow paths with the initiation of snowmelt.

Base cation and DIC concentrations, in contrast, represent a combination of carbonic acid and sulfuric acid weathering of shale carbonates. This balance shows strong seasonal dependence, with sulfuric acid weathering accounting for 75% of base cation fluxes during base flow, and as low as 35% at peak discharge—again dependent on the balance of subsurface flow paths. From this seasonal dependence, we infer that a significant amount of calcite is present in the weathering profile above the pyrite oxidation front and is available for carbonic acid weathering in the shallow/intermediate subsurface. As the progressive deepening of the pyrite oxidation front during regolith formation depletes calcite in the weathering profile through acid-base reactions between sulfuric acid and carbonates, the presence of calcite above the pyrite oxidation front implies that host rock contains significantly less pyrite than carbonate, so that $FeS_2 < 0.25*CaCO_3$ based on stoichiometric balances [*Brantley et al*., 2013]. This is supported by regional characteristics of the Mancos shale, with pyrite and carbonate accounting for 1% and 20% of Mancos by weight percent, respectively [*Morrison et al*., 2012].

It is interesting to note the lack of hysteresis in sulfate concentrations as compared to DIC, base cations, and sulfuric acid weathering percentage, which are all influenced by sulfuric acid weathering. These hysteresis characteristics are then fully a product of changing carbonic acid weathering rates, with faster rates on the rising limb than the falling limb for any given discharge. While to some degree this may represent changing contributions from shallow versus deep flow paths on the rising and falling limbs, shallow flow path end-member concentrations evolve over the course of the snowmelt period as mentioned above and supported by the lack of strong negative correlation between DIC and DOC. Increasing DIC fluxes with discharge means snowmelt waters actively weather carbonate, and lower concentrations on the falling limb relative to the rising limb for a given discharge indicate increasingly shallow and fast transit time flow paths over the course of the snowmelt period. The effect of this is that waters are either unable to penetrate to the carbonate weathering front or are unable to reach calcite saturation in their limited time in the subsurface. In either case, hysteresis of DIC and base cation concentrations is controlled exclusively by carbonic acid weathering, and suggests either that transit times are evolving throughout the snowmelt period or that soil saturation and flushing of bio-available DOC during snowmelt inhibits respiration rates of CO_2 and carbonic acid available

for weathering. Future work will aim to quantify the impacts of nonstationary transit times relative to soil respiration limitations on carbonic acid availability in driving this hysteresis.

Comparing DIC with base cations and sulfate concentrations, we also see that despite a decrease in sulfate and base cation concentrations, DIC is constant to discharges of 1–2 m^3/s. As some proportion of DIC comes from sulfuric acid weathering, this lag in dilution means that absolute contributions of DIC from carbonic acid weathering must increase at these lower discharges. This is shown in Figure 8, in which carbonic acid contributions are calculated by subtracting out the contributions from sulfate weathering ($DIC_{carbonic} = DIC - 2*SO_4$). This seems to imply that concentrations of carbonic acid weathering products increase with increasing discharge—i.e., fluxes will increase faster than 1:1 with discharge—similar to the behavior of DOC. While it is possible that changing conditions of infiltrating water, such as temperature and pCO_2, may alter equilibrium concentrations of dissolved calcite, the degree of increase in weathering rates seems incompatible with decreasing transit times of shallow flow paths implied by DOC, DIC, and sulfate C-Q behavior.

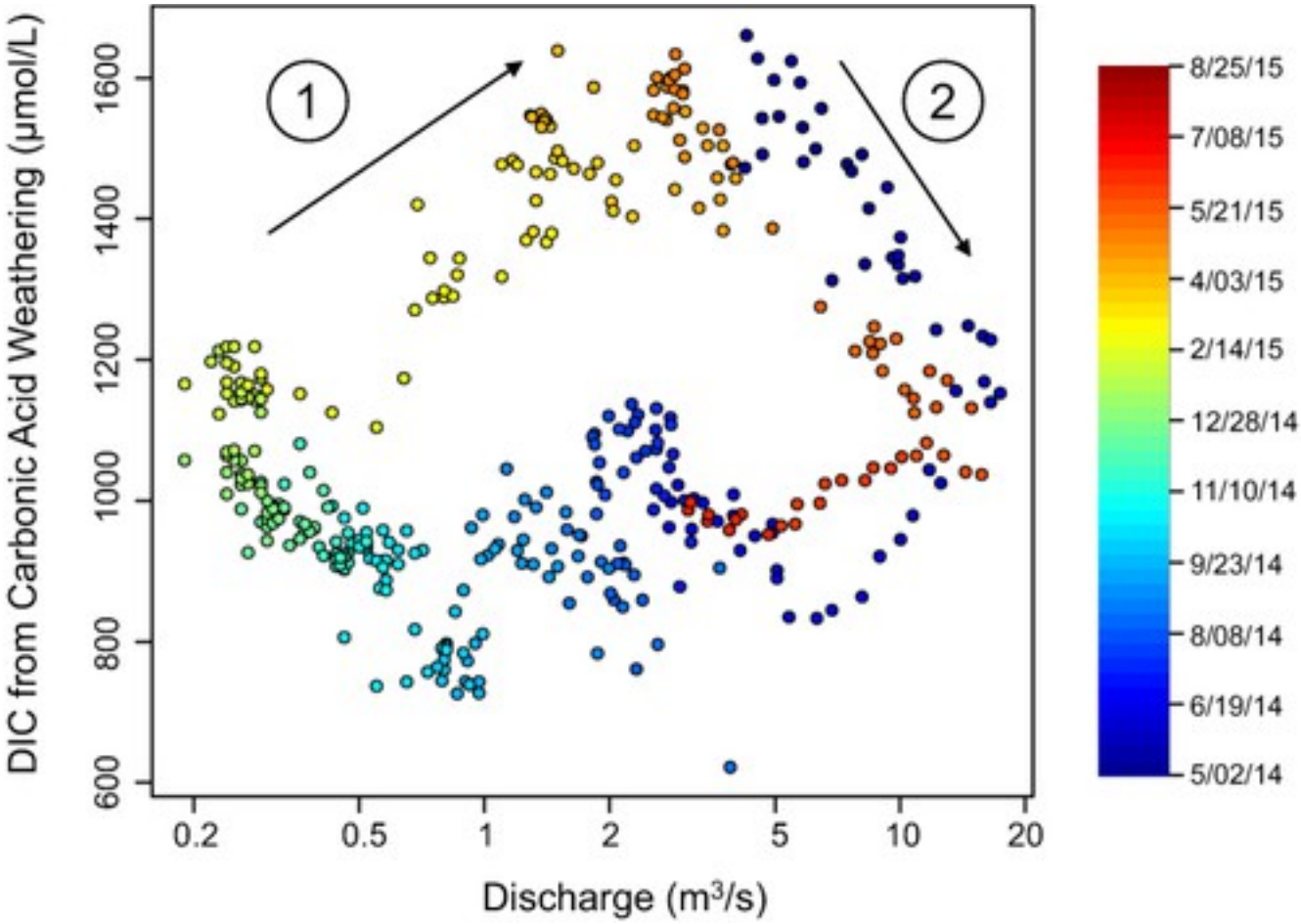

Figure 8

Open in figure viewerPowerPoint

DIC contributions from carbonic acid weathering. Contributions calculated as [DIC] − 2*[SO_4^{2-}] plotted against discharge. Arrow 1 shows increasing contributions from carbonic acid weathering due to decreasing influence of sulfuric acid and arrow 2 shows decreasing carbonic acid weathering contributions due to dilution.

Instead we suggest that during base flow conditions, infiltrating waters reach calcite saturation through carbonic acid weathering. Subsequently, when these calcite-saturated waters pass through the pyrite oxidation front, carbonate alkalinity is reduced while base cation concentrations are maintained. This would occur through the buffering of sulfuric acid by carbonate alkalinity already in solution. If sulfuric acid weathering were instead directly dissolving local carbonate, we would not expect to observe the apparent increases in alkalinity contributions from carbonic acid weathering (Figure 8). Future work will target $\delta^{13}C$ values of DIC and the balance of respiration-derived and rock-derived carbon as an additional constraint on these subsurface reaction networks.

With the initiation of snowmelt, these calcite-saturated waters are unable to reach the pyrite oxidation front, which works to maintain DIC concentrations despite decreasing base cation concentrations. In effect, the passage of waters through the pyrite oxidation front reduces the transport of alkalinity and accounts for the decrease between observed DIC and cation-equivalent concentrations with increasing discharge. This discrepancy, or "missing" carbon constitutes roughly 9.5 tC/km^2/yr, or roughly 33% of the expected annual DIC flux. The increase in CO_2(aq) at the expense of HCO_3^- that occurs during the neutralization of sulfuric acid, results in an increased CO_2 efflux from surface waters as they equilibrate with atmospheric conditions resulting in the "missing" carbon. We demonstrate this conceptual model in Figure 9. While studies have shown that sulfuric acid weathering of carbonates may serve as a transient source of CO_2, our observations of seasonal dynamics show that sulfuric acid weathering actively short-circuits the carbonate weathering cycle by reducing alkalinity exports from calcite-saturated waters.

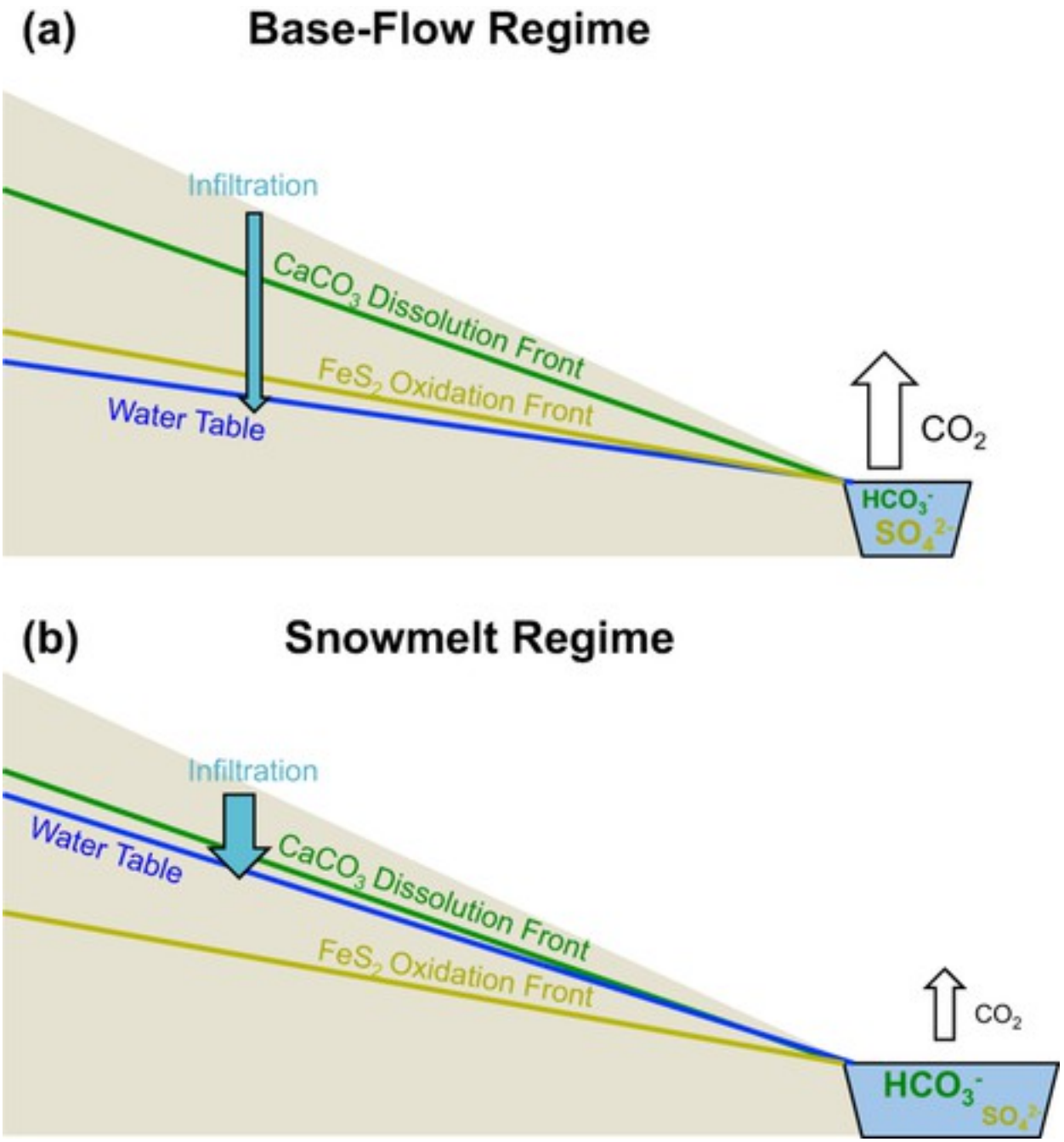

Figure 9

Open in figure viewerPowerPoint

Conceptual model. Infiltration depths are shown relative to inferred subsurface reaction fronts during (a) base flow conditions and (b) snowmelt conditions, along with relative concentrations of HCO_3^- and SO_4^{2-} in surface water and relative CO_2efflux rates.

Finally, the dynamic balance of carbonate weathering between carbonic acid and sulfuric acid from pyrite oxidation may be particularly sensitive to projected changes in snowmelt dynamics. A number of studies of proximal mineralized watersheds have shown increasing sulfate and

contaminant metal concentrations during base flow and in lakes over the past few decades due to systematic deepening of the water table and exposure of subsurface pyrite to oxidative conditions [*Mast et al.*, 2010; *Todd et al.*, 2012; *Manning et al.*, 2013]. The work presented herein demonstrates that the ability of snowmelt waters to infiltrate to pyrite oxidation front depths may also serve as a first-order control on these fluxes and on the balance between carbonic and sulfuric acid weathering, potentially in competition with falling water tables. This is particularly true in the East River where solute fluxes are dominated by snowmelt, so that increasing base flow sulfate concentrations may still be associated with decreased overall sulfate fluxes if snowmelt dilution becomes stronger due to the dominance of shallow flow paths and deepening of the pyrite oxidation front. Additionally, this conceptual model relating hydrologic flow regime and nested reaction fronts to riverine carbon fluxes may be tested within shale-dominated watershed across lowland environments, where large storm events may induce similar effects as snowmelt in the East River. Resolving these dynamics and how they are projected to change in the future will have important implications for downstream water quality and the ability of streams to export alkalinity and carbon with a changing climate.

6 Conclusions

Relationships between concentrations of dissolved solids and discharge can provide unique information regarding integrated watershed processes. We demonstrate that seasonal flow regimes exert a first-order control on C-Q relationships in the East River, CO due to the way in which fluctuating flow paths intersect nested chemical reaction fronts in the subsurface. Under base flow conditions, waters are able to infiltrate to greater depths due to lower water table heights. During infiltration, waters first pass through the calcite dissolution front at intermediate/shallow depths where carbonic acid from soil respiration is neutralized by calcite dissolution. At greater depths, waters pass through the pyrite oxidation front where sulfuric acid is neutralized by HCO_3^- from previous calcite dissolution, increasing CO_2(aq) concentrations. When waters reach the surface and equilibrate with the atmosphere this CO_2 is degassed, resulting in a large discrepancy between HCO_3^- and cation-equivalent concentrations. Conversely during high-discharge snowmelt conditions, rising water tables prevent new water from infiltrating to the pyrite oxidation front, resulting in strong SO_4^{2-} dilution, smaller discrepancies between HCO_3^- and cation-equivalent concentrations, and smaller CO_2 efflux rates from surface waters. Integrated over the annual cycle, the reaction of sulfuric acid with HCO_3^- reduces riverine fluxes of DIC and alkalinity by 33%. This direct control of snowmelt on the ability of the East River to export carbon and alkalinity suggest that carbon cycle fluxes will be particularly sensitive to projected changes in climate. As winter snowpack represents a vital freshwater

resource for much of the globe, increasing our understanding of how snowmelt processes are linked with subsurface biogeochemical reactions will provide better predictive abilities for how climate change may impact water quality into the future. The conceptual model we present also provides a framework that may be applicable within other shale-dominated catchment systems to better characterize variability and projected changes in solute and carbon fluxes.

Acknowledgments

Data used in this study are included in supporting information. We thank Richard Webb and two anonymous reviewers whose suggestions improved an earlier version of this manuscript. We acknowledge the field and logistical support provided by Wendy Brown and the Rocky Mountain Biological Laboratory, Gothic, Colorado. This material is based upon work supported through the Lawrence Berkeley National Laboratory's Watershed Function Scientific Focus Area. The U.S. Department of Energy (DOE), Office of Science, Office of Biological and Environmental Research funded the work under contract DE-AC02-05CH11231 (Lawrence Berkeley National Laboratory; operated by the University of California). Funding to K.M. and M.W. was provided by the U.S. Department of Energy (DOE-DE-SC0014556) and the National Science Foundation (EAR-1254156).